**REVIEW • OPEN ACCESS**

# *In situ* transmission electron microscopy for magnetic nanostructures

View the article online for updates and enhancements.

# Review

# *In situ* transmission electron microscopy for magnetic nanostructures

## Duc-The Ngo[1] and Luise Theil Kuhn[2]

[1] Electron Microscopy Centre, School of Materials, University of Manchester, Oxford Road, Manchester M13 9PL, UK
[2] DTU Energy, Department of Energy Conversion and Storage, Technical University of Denmark, Frederiksborgvej 399, 4000 Roskilde, Denmark

E-mail: duc-the.ngo@manchester.ac.uk

## Abstract

Nanomagnetism is a subject of great interest because of both application and fundamental aspects in which understanding of the physical and electromagnetic structure of magnetic nanostructures is essential to explore the magnetic properties. Transmission electron microscopy (TEM) is a powerful tool that allows understanding of both physical structure and micromagnetic structure of the thin samples at nanoscale. Among TEM techniques, *in situ* TEM is the state-of-the-art approach for imaging such structures in dynamic experiments, reconstructing a real-time nanoscale picture of the properties–structure correlation. This paper aims at reviewing and discussing *in situ* TEM magnetic imaging studies, including Lorentz microscopy and electron holography in TEM, applied to the research of magnetic nanostructures.

## 1. Introduction

Magnetic materials and devices play vital roles in engineering and technology. In solid state physics and materials science, magnetism is a subject of great interest where the magnetic properties of the materials are explored to produce electronic devices based on the magnetism. Great efforts are being made in science and technology to create a new generation of electronic devices based on magnetism called spin electronics, or spintronics, in which both charge and spin of the electron can be exploited [1, 2]. The Nobel Prize in physics 2007 for A Fert and P Grünberg for the discovery of giant magnetoresistance marked an important developing step of spintronics as well as magnetism and magnetic materials [3, 4]. Together with the emerging of nanoscience and nanotechnology, nanomagnetism has shown new magnetic properties and applications. Nanomagnetism is the discipline dealing with magnetic phenomena dedicated to structures whose dimensions are in the submicron scale. The scientific challenges in nanomagnetism involve [5]: (i) creating new magnetic nanostructures with special properties, (ii) understanding physical structure and micromagnetic structure as well as its behaviours by structural analysis techniques to tailor the structure and properties for new applications. This paper will focus on reviewing the approach to resolve the second challenge in nanomagnetism with the application of a state-of-the-art tool for magnetic structure analysis, magnetic imaging in transmission electron microscopy (TEM) with *in situ* experiments.

TEM is a powerful imaging and analysis tool which has been widely used over the world for many decades. TEM is known as a microscopy technique whereby an electron beam transmits through an ultrathin specimen, interacting with the specimen to form highly magnified images. The high energy electron beam (commonly 80–300 kV, or even up to 1200 kV)

creates very short electron wave (below 1 pm) which allows sub-nanometer scale structure to be resolved using magnetic lenses [6–8]. Nowadays, with the development of electron sources and magnetic lenses, TEM belongs to the best nanoimaging techniques with spatial resolution down to sub-angstrom level [8]. Together with the capability of ultrahigh resolution imaging, interaction of the high energy beam and the sample results in characteristic spectroscopies such as energy dispersive x-ray spectroscopy (EDX/EDS), and electron energy loss spectroscopy (EELS) which are very helpful for nanoanalysis of chemical composition, bonding as well as chemical structure [7, 9]. Based on the deflection of electron beam in electromagnetic field, magnetic and electric fields in the specimen could be imaged in TEM using Lorentz microscopy or electron holography [10, 11]. These techniques nowadays are among the best magnetic imaging methods in terms of spatial resolution as well as capability of additional experiments.

In this article we focus on reviewing the TEM techniques applied for imaging magnetic structures in nanostructures in terms of performing *in situ* magnetic experiments.

## 2. Technique and equipment for magnetic imaging in TEM

Magnetic imaging in TEM (Lorentz microscopy) is based on deflection of the electron beam by the Lorentz force as transmitted through the specimen:

$$\mathbf{F_L} = -e[\mathbf{E} + (\mathbf{v} \times \mathbf{B})], \tag{1}$$

where $e$ and $\mathbf{v}$ are the electron charge ($1.6 \times 10^{-19}$ C) and electron velocity; $\mathbf{E}$ and $\mathbf{B}$ are the electric field and magnetic induction, respectively. If we consider a parallel beam which is incident perpendicular to the specimen plane (along the $z$ axis), the angle of deflection due to the Lorentz force is given by [10]

$$\beta_L = \frac{e\lambda}{h} \int_{-\infty}^{+\infty} B_{\perp}(x, y)dz, \tag{2}$$

where $B_{\perp}(x,y)$ is the in-plane component of magnetic induction at point $(x, y)$, $\lambda$ is the electron wavelength, $h$ is the Planck's constant. Approximately, if stray field effects are ignored, the magnetisation ($M_s$) is considered uniform and the specimen has a constant thickness, $t$, the equation (2) can be simplified as:

$$\beta_L = \frac{e\lambda B_s t}{h}. \tag{3}$$

For example, an electron beam accelerated by a voltage of 200 kV transmitted through a 20 nm thick specimen with a saturation induction $B_s = \mu_0 M_s = 1$ T, the deflection angle $\beta_L$ will be about $1.2 \times 10^{-5}$ rad which is much smaller than the angle of Bragg diffraction (order of $10^{-2}$ rad) commonly seen in normal TEM. Such a small deflection angle could only be detected and focused by a mini-Lorentz lens placed far below the specimen, further down than the standard objective lens.

The above description is based on classical mechanics approach which makes image calculation difficult. It can be overcome by taking a quantum mechanics point of view in which the electron beam is considered as a wave and the
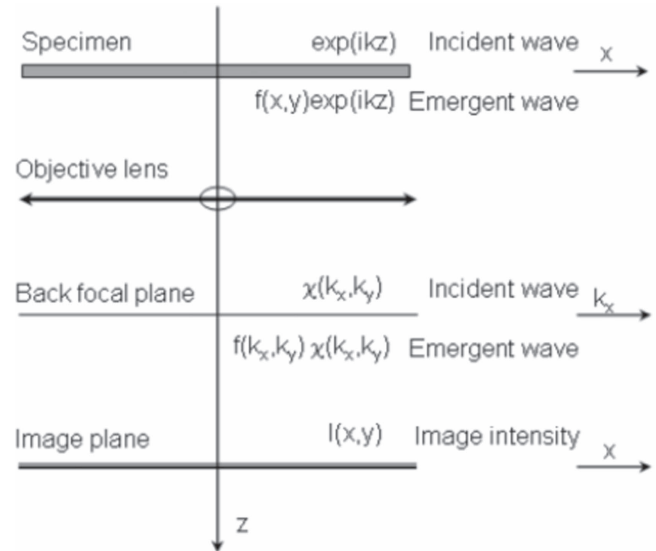


**Figure 1.** Image formation of magnetic structure in conventional TEM [12]. The figure is reproduced under permission of the thesis author (D-T Ngo).

specimen is a phase object, and the imaging in Lorentz microscopy is considered as wave propagation (figure 1) [12]. As passed through the specimen, the phase of the electron wave is shifted an amount of $\phi$. This phase shift may include a magnetic component due to the interaction with magnetic vector potential ($A$), and electrostatic component induced by electrostatic potential $V$ [12]

$$\phi(x, y, z) = \frac{e}{\hbar c} \int_{-\infty}^{z} V(x, y, z)dz - \frac{e}{\hbar} \int_{-\infty}^{z} \mathbf{A}(x, y, z)d\mathbf{z}. \tag{4}$$

If the sample is purely magnetic, the electrostatic component is simply written as:

$$\phi_e = \frac{\pi V t}{\lambda E_k}, \tag{5}$$

$E_k$ is electron beam energy, and the magnetic phase shift is given by:

$$\phi_m(x, y) = -\frac{e}{\hbar} \int_{-\infty}^{+\infty} (\mathbf{B}(x, y) \times \mathbf{n_z})dz$$
$$\approx -\frac{e}{\hbar}(\mathbf{B_{\perp}} \times \mathbf{n_z})t. \tag{6}$$

The wave function of the electron beam existing from the specimen is written as [12]

$$\varphi(r) = A(x, y) \exp\{i(kz + \phi(x, y, z)\}. \tag{7}$$

Here $A(x, y)$ is the amplitude function, $k = 2\pi/\lambda$ is the wave number. The microscope term could be included as a transfer function ($TF$) and aperture function ($APF$), and the complex wave function at the back focal plane of the imaging lens will be given by [12]

$$\Psi(k_x, k_y) = FT[\varphi(r)] \times \exp\{i\, TF\} \times APF, \tag{8}$$

Adv. Nat. Sci.: Nanosci. Nanotechnol. **7** (2016) 045001

Review
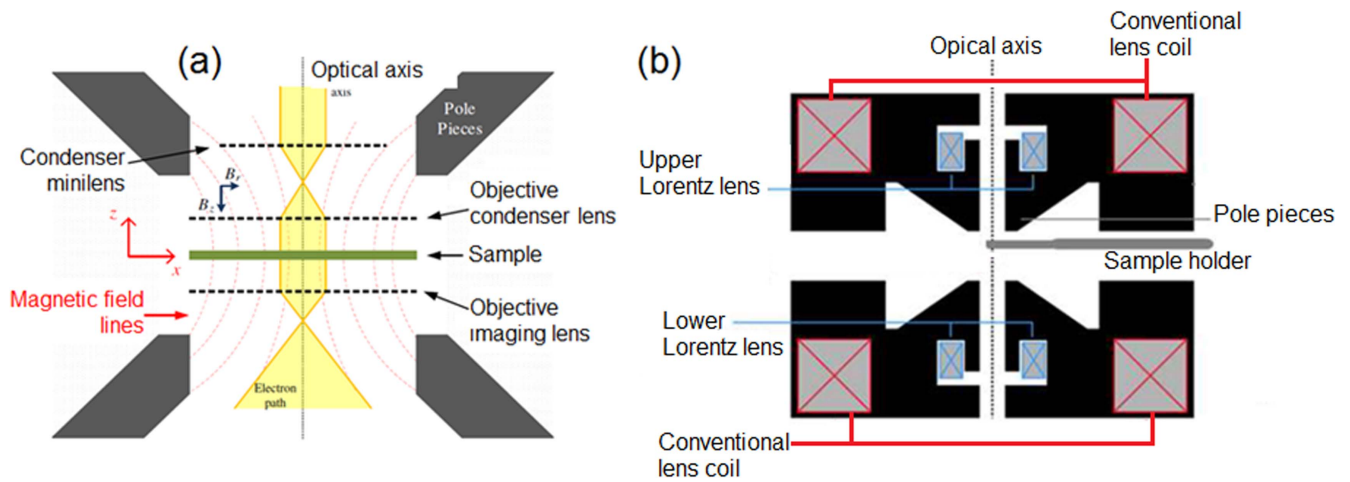


**Figure 2.** (a) Standard objective lens in TEM: specimen is immersed in strong magnetic field [14], (b) modified objective lens for field-free environment and mini Lorentz lens for magnetic imaging in Philip CM20. Figure is reproduced under permission by Elsevier.

in this case, *FT* denotes the Fourier transform operator. In magnetic imaging TEM, APF is a top-hat function having value 1 inside its radius and 0 outside, whereas the transfer function is a function of the spatial frequency ($K$):

$$TF = \pi \Delta f \lambda K^2 + \frac{\pi C_s \lambda^3 K^4}{2}, \qquad (9)$$

where $\Delta f$ is the defocused level of the imaging lens, $C_s$ is spherical aberration of the imaging lens which may be up to 8000 mm in a common Lorentz mini-lens [12].

It is well-known that the image in TEM is formed using a system of magnetic lenses in which the objective lens plays the most important role for magnifying and focusing. Commonly, the standard objective lens generates a strong magnetic field (up to 2.2 T in most TEMs) which could either saturate or distort magnetic structure of the sample immersed in the objective lens (see figure 2(a)). Therefore, magnetic structure could not be observed in standard TEM equipment. To generate magnetic contrast in TEM imaging, a perfectly field-free medium in objective lens is required to immerse the specimen. A number of efforts have been made to overcome this challenge. One of the most common modifications is to switch the standard objective lens to remain the field-free medium, and it was developed by the research group at Glasgow led by Prof. John Chapman [10, 13]. In this situation, the mini-lens (Lorentz lens) was used as an additional objective lens for imaging (see figure 2(b)) [12] and Lorentz TEM (LTEM) can be constructed.

The most common LTEM is available in conventional TEM (CTEM) in which a parallel electron beam is used: the Fresnel mode and the Foucault mode (figure 3). Figure 3 represents the mechanism of magnetic contrast for a simple specimen containing domains magnetised in the plane of the film and separated by 180° domain walls. The Lorentz force present as a result of the magnetic domains deflects the electrons passing through the specimen and splits each of the diffraction spots (by the magnetic domains) into two. Each split spot contains information of the magnetic induction from domains in which magnetization is lying.

In the Fresnel imaging mode, the image-forming lens (mini Lorentz lens) is defocused so that an out-of-focus image of the specimen is created. The magnetic domain walls are then visible as alternating bright and dark lines. The domain wall contrast can be changed between dark and bright by changing the sign of the defocus (figure 3). If a coherent electron source is used, the convergent wall images may consist of sets of fringes running parallel to the wall, which allow detailed information about the domain wall structure to be analysed [16]. Information about the magnetisation direction within the magnetic domains can also be quantified by analysing the magnetization ripple in the Fresnel images if the sample is polycrystalline [12, 17]. The advantages of Fresnel imaging for studying magnetic specimens are its ease of operation and the high levels of contrast. It is also easy to perform real-time *in situ* imaging, allowing reversal sequences to be recorded during magnetising experiments. Fresnel imaging allows observation of the behaviour of walls under external fields, the domain wall shape, magnetic domain geometry, etc. (magnetising experiments). However, Fresnel imaging is very limited for quantification of the magnetic structure of films because of limited resolution (above 20 nm for a good visibility) [12].

Another Lorentz imaging mode in CTEM is Foucault mode (figure 3) in which the imaging lens is kept in-focus but one of the split spots in the diffraction pattern is covered by displacing an aperture in the focal plane where the diffraction pattern is formed. The contrast will result from the magnetization within the magnetic domains. The domains that electrons are deflected through the aperture appear bright whereas the domains with the magnetisation aligned antiparallel to this magnetisation direction of the bright domains will appear dark. The direction of magnetisation in the domains would be then determined if the relative direction of aperture displacement with respect to the image is known. The contrast in Foucault images is very sensitive to the position of the aperture; therefore the technique is not quantitative if only a single pair of Foucault images is recorded along each aperture
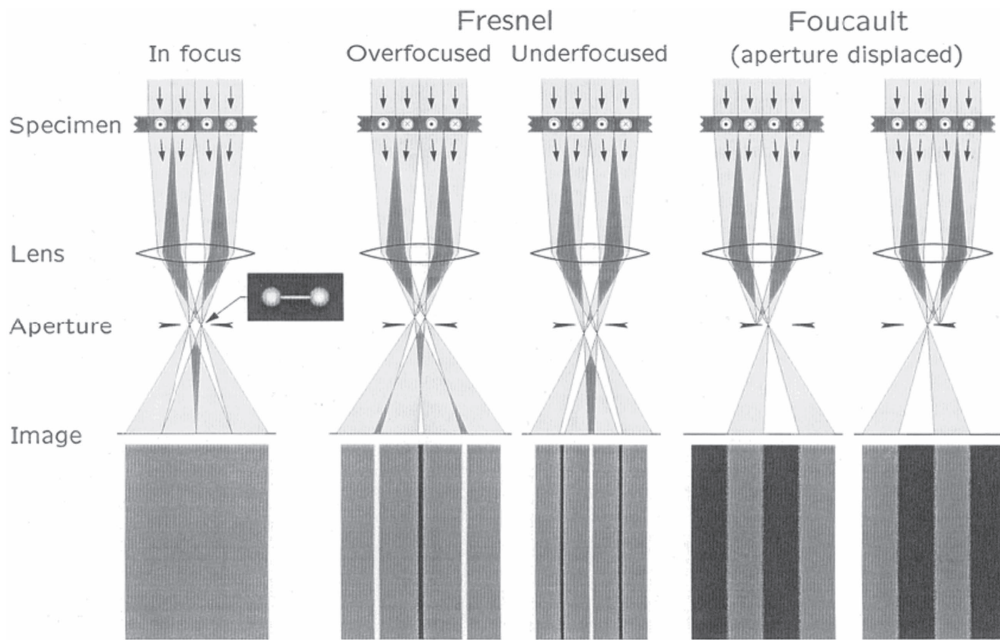
**Figure 3.** A schematic diagram representing the origin of the Lorentz deflection in a TEM for a magnetic film containing domains magnetized in two directions. Fresnel images are obtained by overfocusing or underfocusing the objective lens; Foucault images are obtained by displacing the objective aperture [15]. Figure is reproduced under permission of Springer.
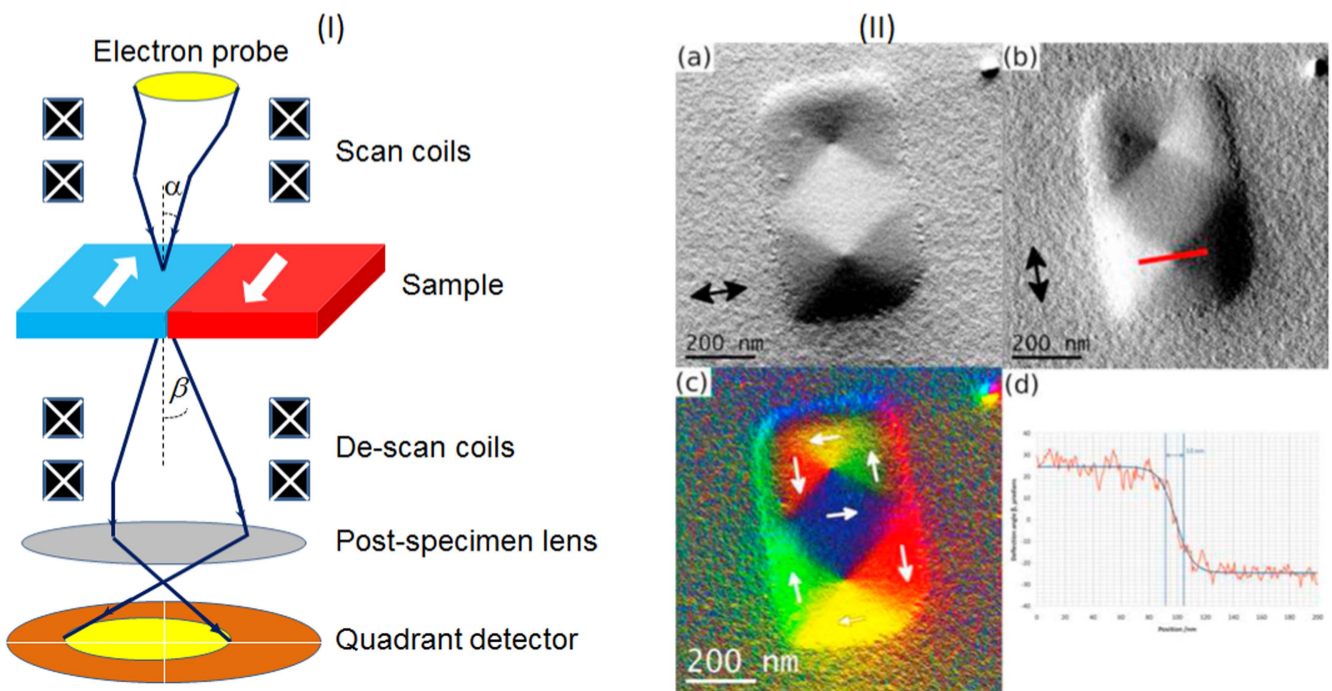


**Figure 4.** (I) Principle of the DPC technique in Lorentz STEM, and (II) DPC image components [19]. (a) horizontal magnetic induction, (b) vertical magnetic induction, (c) reconstructed total magnetic induction, (d) Linetrace from image (b) showing the induction profile, as a measured deflection angle in microradians. The figure is reproduced under permission Elsevier.

displacement direction. The best resolution of 5–6 nm was demonstrated by Podbrdsky in 1974 [18].

The best resolution in Lorentz microscopy can be obtained in scanning TEM (STEM) where the differential phase contrast (DPC) mode was introduced and developed by Chapman *et al* at the first time in 1978 [20]. Differential phase contrast (DPC) in LTEM is a high-resolution magnetic

imaging technique for visualising the distribution of magnetic induction in thin samples carried out in STEM by using a focused electron beam as a probe scanning on the sample. The DPC technique, principally described in figure 4, requires a field emission gun source to create a very high monochromatic electron beam that is converged as a probe by a probe forming aperture. The probe is scanned across the specimen

by scanning coils similar to those in normal STEM. After transmission through the specimen, the electron beam emerges as a cone of illumination which will be projected onto a circular quadrant detector. If the specimen is non-magnetic, the disc will be centred on the detector. If the specimen is magnetic, the Lorentz force will deflect the electrons and shift the disc to a position that is no longer concentric on the detector. Using de-scan coils, the beam remains stationary with respect to the detector whilst scanning which ensures that deflections caused by the magnetic induction are the only shifts of the beam from the central position. Each segment of the detector measures a separate electron signal. The difference signals taken from opposite segments on quadrants will provide information on the induction as two orthogonal components. Besides, the sum of the signals from the four quadrants also produces a bright field image of the specimen. The difference signal, $S$, is approximately proportional to the magnetic induction, $B_s$, in the specimen as follows:

$$S = \frac{4IeB_s\lambda t}{\pi \alpha h}, \tag{10}$$

here $I$ is the electron beam intensity, $\alpha$ is convergent angle of the beam. This relation allows interpretation of the magnetic induction in the specimen in DPC LTEM to be straightforward. The resolution in DPC LTEM depends on the probe size. As using probe-forming aperture and upper Lorentz lens to create the probe, the probe size could not be as small as in normal STEM, which could be Angstrom scale. Therefore, the best resolution in DPC LTEM was commonly achieved in range of 2–5 nm [12, 13, 21], which is of the best among magnetic imaging techniques. Recently, using aberration-corrected STEM, the best resolution of DPC Lorentz STEM up to 0.9 nm has been reported by McVitie *et al* [19].

High resolution, straightforward interpretation and easy mapping of magnetic induction are the main advantages of DPC LTEM. As the technique is based on scanning mode, it takes longer time to record an image than Fresnel and Foucault imaging. Furthermore, relation (10) indicates that the difference signal decreases with increasing the convergent angle, $\alpha$. On the other hand, when the larger convergent angle is used, the smaller probe is obtained. Therefore, the signal becomes weaker at higher resolution for DPC LTEM.

Another magnetic imaging technique in Lorentz TEM is electron holography which was introduced by Dennis Gabor in 1948 [23], and demonstrated firstly by Haine and Mulvey in 1952 [24]. However, electron holography has only become widely available on commercial TEM recently. Although there are several variants of electron holography, including in-line and scanning TEM-based electron holography [25, 26], the most commonly-used method is the TEM mode of off-axis electron holography described in figure 5.

The most important requirement for electron holography is a coherent source of electrons. In fact there is no a perfectly coherent electron source, either spatially or temporally, but the degree of coherence must be such that an interference pattern of sufficient contrast and intensity can be recorded on a negative, image plate or CCD camera within a reasonable acquisition time to avoid specimen drift and/or beam drift. A

cold field-emission gun (FEG) is such a sufficiently coherent source to be used in electron holography. When the electron wave passes through the sample, the phase shift in the exit wave contains information of magnetic and electric fields in the sample as described in equations (6)–(8). An electron biprism inserted between the back focal plane and the image plane superimposes the exit wave and the incident wave resulting in an interference pattern (hologram) observed in the image plane. From the hologram, the electron wave can be reconstructed in the form of two images, an amplitude image and a phase image. The phase image provides us information of the electric and magnetic fields as described in equations (4)–(6). Considering a magnetic sample with uniform thickness, the components of the magnetic induction inside the sample can be mapped from the reconstructed phase based on the relation in equation (6) [27]

$$B_x(x, y) = \frac{\hbar}{e.t} \frac{\partial \phi(x, y)}{\partial y} \text{ and } B_y(x, y)$$
$$= -\frac{\hbar}{e.t} \frac{\partial \phi(x, y)}{\partial x}. \tag{11}$$

Depending on the quality of the phase reconstruction algorithm, electron holography can image magnetic structure with high resolution up to 1–2 nm. But it should be noticed that electron holography requires an algorithm to recover the phase information from the hologram, commonly based on Fourier transform. Besides, field view in electron holography seems to be limited and it needs to position the specimen close to vacuum, which may influence the micromagnetic structure due to stray fields [28].

## 3. Applications of *in situ* TEM for magnetic nanostructures

One of the main reasons to use TEM for magnetic imaging is that it enables possibilities of performing *in situ* magnetodynamic experiments inside the TEM. In parallel with high-resolution imaging, *in situ* experiments help to correlate the physical structure, magnetic structure with magnetic properties, especially, at atomic scale level. This makes the TEM a 'mini magnetic laboratory' to study nanomagnetism.

### 3.1. Dynamics of magnetisation reversal process in LTEM chamber

One of the greatest interests is the ability to conduct *in situ* observations of the magnetization reversal process by applying a controlled magnetic field during imaging. In Lorentz TEM, the mini Lorentz lens is used as imaging objective lens and the objective lens can be used to introduce a controllable vertical field [12, 13, 16]. This is realised by weakly exciting the lens coils to produce a magnetic field, $H$, parallel to the optical axis, or perpendicular to the specimen plane. To create the in-plane field parallel to the specimen, the specimen is tilted at an angle, $\theta$, and the magnitude of the in-plane field is $H \sin\theta$ [12]. The second method to apply a magnetic field to
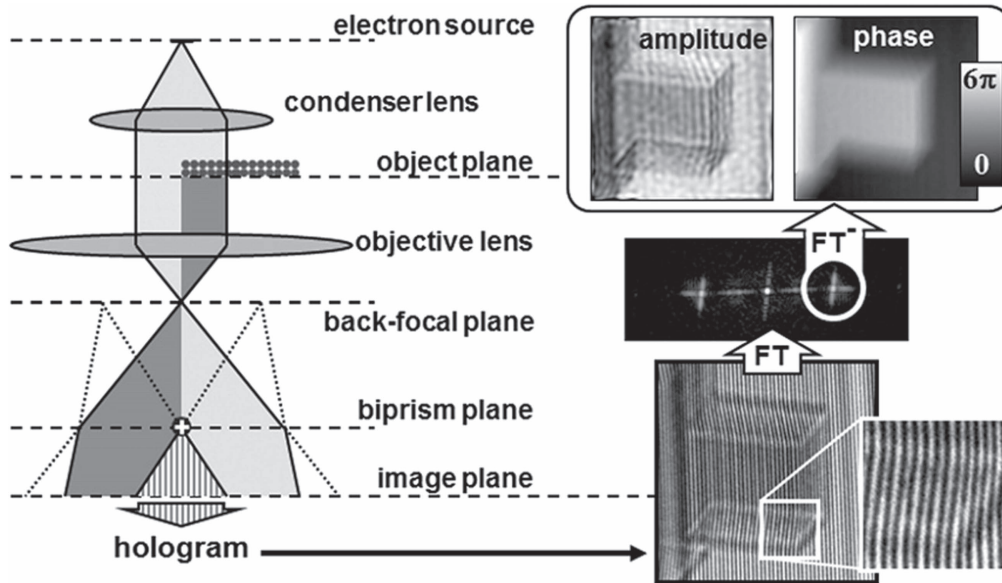
**Figure 5.** Principle of electron holography in TEM: (left) experimental setup, (right) an example of a hologram of a MgO crystal illustrates the holographic reconstruction in that the complex image wave is retrieved by Fourier transform [22]. The figure is reproduced under permission by Elsevier.
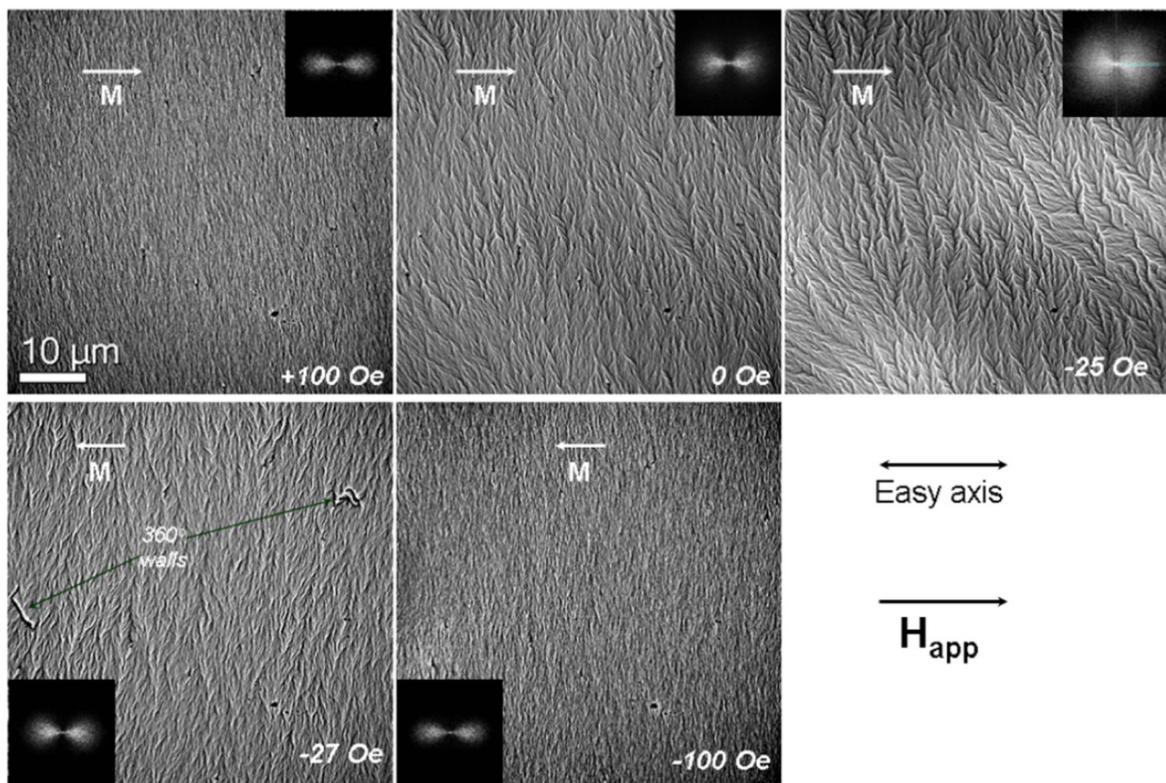


**Figure 6.** *In situ* LTEM study of magnetisation reversal in $Co_{80}Ir_{20}$ film: Fresnel images in a hysteresis sequence on the easy axis in plane of the film. The insets show the Fourier transform of Fresnel images reflecting the dispersion level of the magnetisation ripple. The images were recorded in a Philip CM20 TEM with a FEG [37]. The figure is reproduced under permission of IOP Publishing.

the sample during magnetic imaging is to use an electro-magnet to generate a magnetic field, either built into the specimen holder [29, 30], or situated in the TEM column at the specimen height [31, 32]. This method could allow a horizontal (in-plane) field to be introduced to the specimen plane but there is an issue of deflection of the electron beam by the horizontal field. This deflection results in increasing distortion of the image and ultimately in the illumination disappearing from the field of view above a certain critical field value unless the beams tilt is corrected [16].
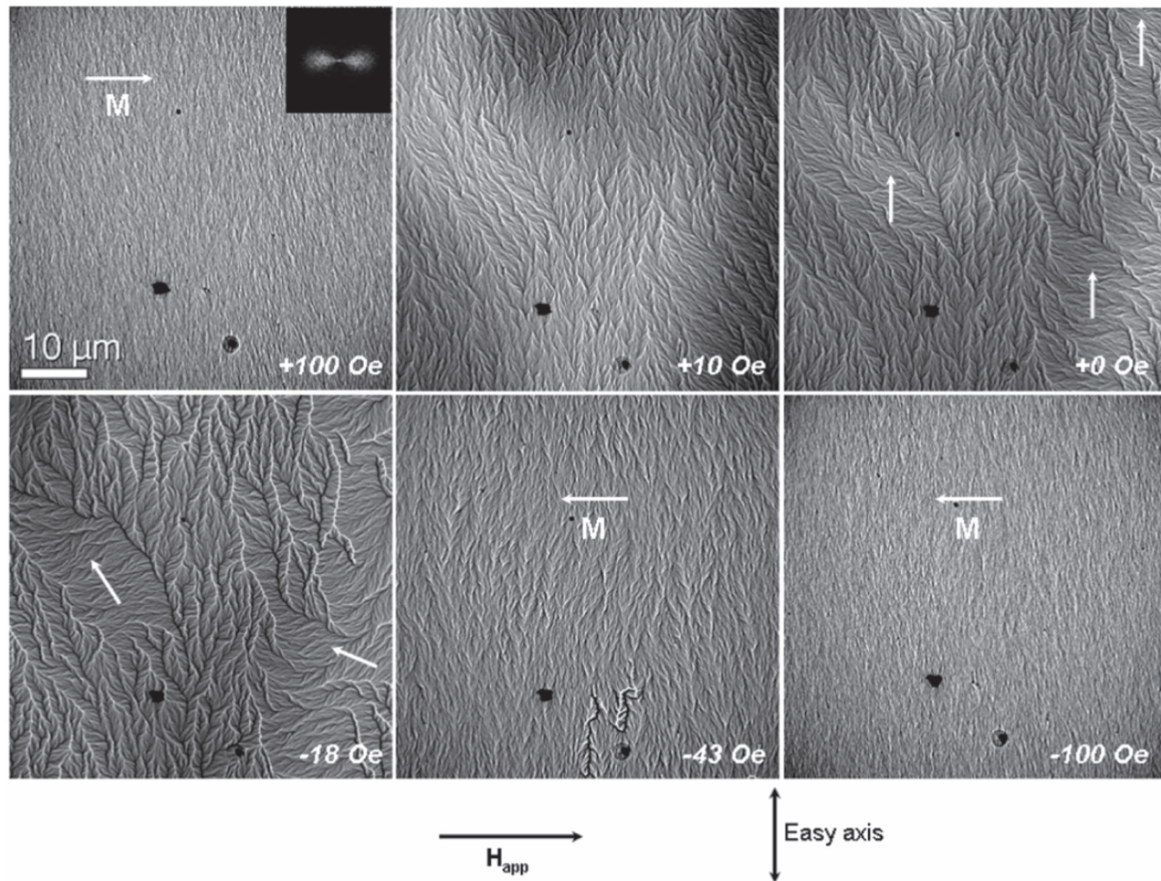
**Figure 7.** *In situ* LTEM study of magnetisation reversal in $Co_{80}Ir_{20}$ film: Fresnel images in a hysteresis sequence on the hard axis in plane of the film. The images were recorded in a Philip CM20 TEM with a FEG [37]. The figure is reproduced under permission of IOP Publishing.

Application of *in situ* LTEM to study magnetisation reversal process in continuous films has been extensively reported [33–37]. The most common way for electron transparency was to deposit the films on a TEM substrate, which is a lithographically fabricated Si substrate supported by a thin SiN window for electron transparency [12]. Figures 6 and 7 illustrate magnetisation reversal on easy and hard axes of $Co_{80}Ir_{20}$ film grown on a Ru buffer layer observed by *in situ* Fresnel imaging of LTEM [37].

On the easy axis (figure 6), the magnetic structure is typically identified by picture of a magnetisation ripple perpendicular to the direction of the magnetisation. The dispersion of the magnetisation ripple appears to be minimised at the saturation field, and starts increasing as reversing the field to the opposite direction. Maximum dispersion of the ripple is observed at the switching field due to a domain wall was seen to rapidly sweep through the film effecting reversal leaving a nearly uniform but oppositely directed magnetization. Thus, the switching field is measurable from this reversal manner as $27 \pm 2$ Oe. It is obviously seen that the reversal mechanism along the nominal easy axis is essentially governed by domain wall nucleation and movement. The magnetic moments align along the easy axis, and it is apparent that the magnetisation reversal was initialized by nucleating a reversed domain with an associated domain wall sweep through the film. It should be noted that the wall swept so fast

that it could not be captured by the CCD camera. Instead it was only visible as a sudden movement on the viewing screen of the microscope.

Differently, the magnetisation reversal on the hard axis (perpendicular to the easy axis) can be identified by gradual formation and movement of low-angle walls caused by the magnetisation rotation when the field was reversed from positive saturation to negative saturation field (figure 7). This process is apparently different from reversal mechanism on the easy axis where the wall was nucleated and swept very quickly at the switching field. The reversal in the hard axis of the studied $Co_{80}Ir_{20}$ film is essentially governed by the mechanism of non-coherent rotation of the magnetization. This is a slightly different from 'conventional' hard-axis reversal where the process is commonly a coherent rotation to form uniform ripple spectrum or low-angle wall structure. On the hard axis, when the field is reduced to zero, the magnetization is relaxed to the easy axis direction by non-coherent rotation of the magnetic moments resulting in the formation of a number of magnetic domains in which the magnetisation aligns to the easy axis. Increasing the applied field to the opposite direction, the magnetic moments rotate from the easy axis to the hard axis. The low-angle walls are as a result formed during such a non-coherent rotation. The hard axis is additionally identified by a smaller coercive field (in this case, 18 Oe) than for the easy axis at which
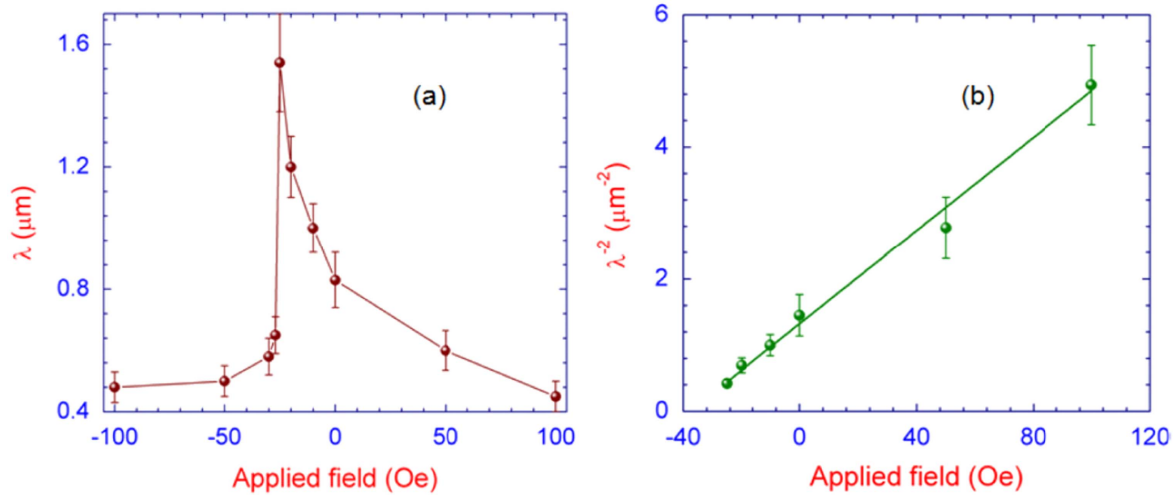
**Figure 8.** *In situ* characterisation of micromagnetic behaviour in $Co_{80}Ir_{20}$ film from Fresnel images [37]: (a) the variation of the mean wavelength in hysteresis process in reversal from $+100$ to $-100$ Oe; (b) the linear dependence of inverse wavelength square on the magnetic field. The figure is reproduced under permission of IOP Publishing.

maximum density of the walls is observed. Another notable observation in the reversal *in situ* experiment is the presence of 360° walls, which occurs in the film during the reversal processes on both easy and hard axes (for example in figure 6 at $-27$ Oe and also in figure 7 at $-43$ Oe). This type of magnetic domain wall, which is energetically unfavourable, is a result of the singularities in 180° walls (Bloch or Néel lines), which are trapped at an inclusion in a magnetizing axis, such as defects, or stacking faults or layer roughness in the film [38]. The 360° walls are hard to remove by the applied field therefore they resist the magnetic saturation, and this process could only be detected by the micromagnetic observation instead of other magnetometric measurements.

Another interesting point of the *in situ* imaging of magnetisation reversal using Fresnel imaging is the magnetisation ripple from which further micromagnetic behaviour of the film could be understood. In this case, the studied $Co_{80}Ir_{20}$ film is polycrystalline; therefore, the contrast of wave-like magnetic ripple is visible in the Fresnel image (see figure 6 as a typical picture). The magnetic ripple can be characterized in terms of the mean wavelength and the mean angle of deviation of the local magnetization which can be measured using Fourier transform of the Fresnel image [12, 37]. During the magnetisation reversal, the mean wavelength varies as a function of the applied field in the form according to the ripple theory [39]

$$\lambda(h) = 2\pi (A/K_u)^{1/2}(h + 1)^{1/2}, \qquad (12)$$

where $A$ is the exchange constant of the material, $K_u$ is the uniaxial anisotropy constant, and $h = H/H_k$ is the reduced magnetic field ($H$ is the magnetic field, $H_k$ is the anisotropy field). This relation can be written as

$$\lambda(h)^{-2} = \left[2\pi \left(\frac{A}{K_u}\right)^{1/2}\right]^{-2}\left(\frac{H}{H_k} + 1\right) \qquad (13)$$

Figure 8(a) shows mean wavelength of magnetisation ripple in $Co_{80}Ir_{20}$ film varying as a function of the applied field during the reversal process recorded on LTEM. In consistency with visibility in the Fresnel images, the wavelength reaches maximum at the switching field where the maximum level of ripple dispersion is observed in the Fresnel image. Using the relation (13), the anisotropy field, $H_k$, of the film is deduced using the linear dependence of $\lambda(h)^{-2}$ on the applied field, $H$ as shown in figure 8(b). This is an effective method to determine an important micromagnetic parameter of the magnetic field: the anisotropy field (in this case, $40 \pm 3$ Oe for $Co_{80}Ir_{20}$ film), and the method was confirmed to be consistent with magnetometric measurements [37].

In addition, application of *in situ* LTEM to study dynamic magnetisation in lithographically patterned nanostructures is an important approach in micromagnetic research [12, 14, 40–43]. Different from continuous film, micromagnetic behaviour of the patterned nanostructure depends on their size, shape, thickness, and microstructure of the element, therefore spatially resolved quantitative magnetic characterization is highly desired. Figure 9 presents an *in situ* LTEM study of magnetisation dynamic in a NiFe patterned film containing a nanobrigde to trap the magnetic domain walls. An interesting feature of Fresnel image of the patterned element is the possibility to determine direction of magnetisation from the edge contrast [40]. For example, at the saturation state (figure 9(a)) thick dark fringes at the bottom edges and thin top edge fringes of the two pads indicate that they are both magnetized in the same direction, parallel to the easy axis direction (white arrow in the figure). When the magnetisation of the elliptical pad is switched (figures 9(d) and (e)) the contrast at the top edge of the pad appears dark. Switching of the elliptical pad results in a formation of a magnetic domain wall (figure 9(d)), and it is driven to be pinned at the nanobridge by the applied field. Using high resolution STEM-DPC mode, confinement of the wall inside
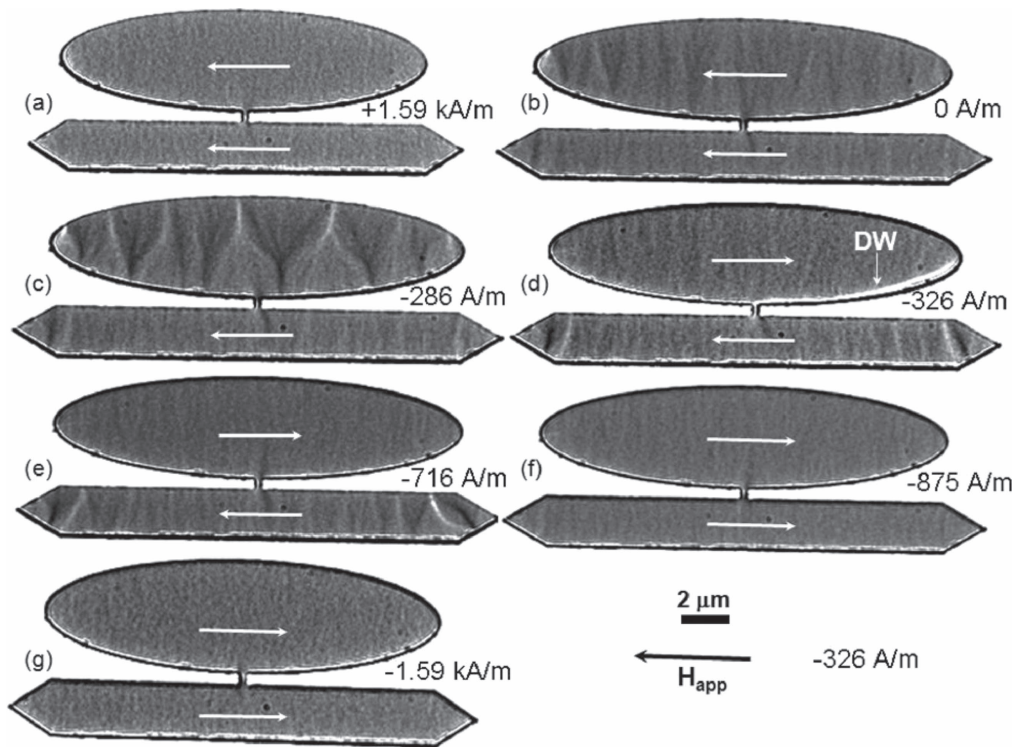
**Figure 9.** Dynamic of a magnetisation reversal in NiFe patterned film observed by *in situ* LTEM [40]. Fresnel images of the structure with a 200 nm × 280 nm nanoconstriction connecting two microsized pads during demagnetization at various magnetic fields: (a) 1.59 kA m$^{-1}$, (b) 0.0, (c) 286 A m$^{-1}$, (d) 326 A m$^{-1}$, (e) 716 A m$^{-1}$, (f) 875 A m$^{-1}$ and (g) 1.59 kA m$^{-1}$. The white arrows denote magnetisation and black arrow denotes the applied field. Reproduction permitted by IEEE Xplore.
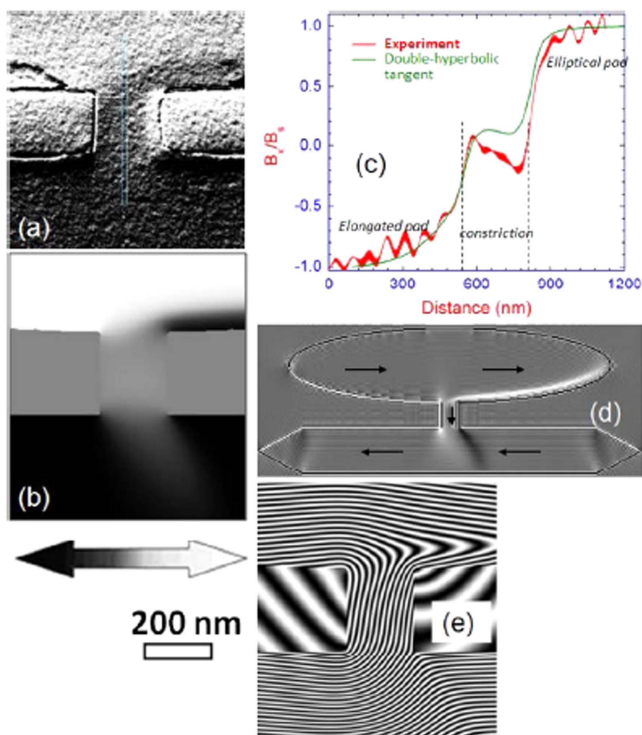


**Figure 10.** DPC images of NiFe constriction at the wall pinning state (state shown in figure 9(d)): (a) experimental image recorded at 326 A m$^{-1}$, (b) simulated image, (c) 20-lines induction profiles in the structure, (d) out-of-plane magnetization curl component, and (e) simulated induction flux calculated from electron phase [40]. Reproduction permitted by IEEE Xplore.

the nanobridge due to geometric constraint is observed (figure 10).

Confinement of the wall with complex structure (see high resolution imaging of the wall structure shown in figure 10) causes a strong scattering on the conduction electrons resulting in a high magnetoresistance reported previously [44]. It is interesting to note that the origin of the large magnetoresistance effect in such a device could only be understood by using high resolution magnetic imaging techniques like LTEM, and the *in situ* experiment allows explaining exactly the dynamic properties of the device under magnetisation reversal.

### 3.2. In situ magneto-electric measurement in LTEM

Magnetotransport in magnetic nanostructure is an important subject of nanomagnetism for magnetoelectronics. Magnetotransport properties of magnetic nanostructures are essentially governed by the interaction of electron/spin current and the micromagnetic structure. And *in situ* measurement of magneto-electric properties in TEM magnetic imaging could help to describe this aspect [45–47]. Developments of TEM sample holders have enabled a new field of research in the study of functional nanomaterials and devices via electrical stimulation and measurement in TEM, particularly in TEM magnetic imaging [48].

In order to perform magnetotransport measurement in LTEM, a specimen holder capable of electrical measurement (biasing holder) is required. The biasing holder allows
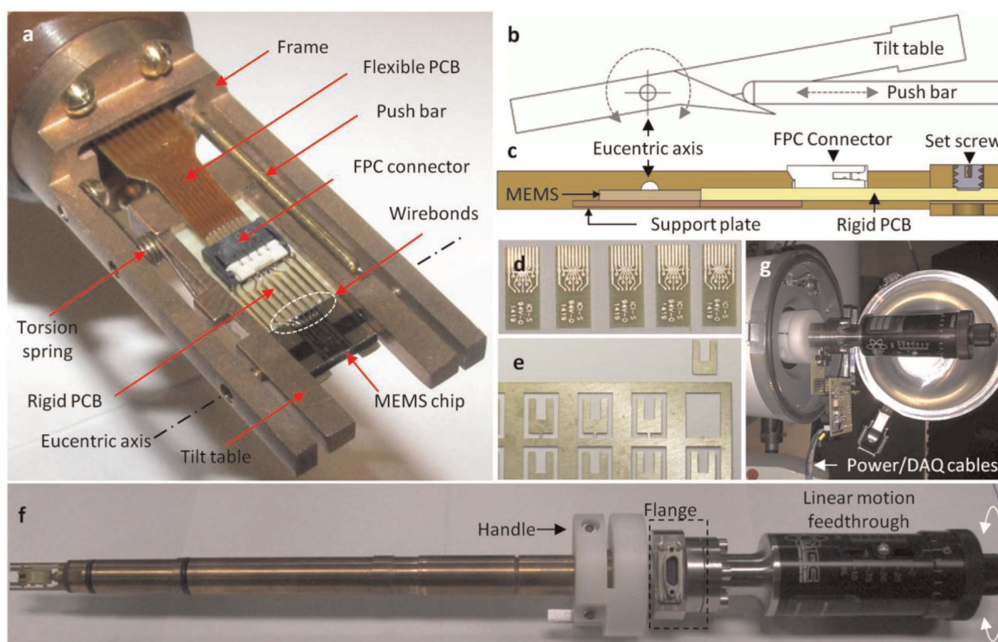
**Figure 11.** A double-tilt holder for Jeol TEM developed by Bernal *et al* [49]: (a) sample stage with contacts for electrical measurements, heating and tilting, (b) and (c) mechanical features for tilting and MEMS experiments, (d) and (e) electrical contacts, (f) picture of whole holder, (g) holder in TEM compustage. Reproducing permission by Elsevier.

electrical voltage/current to be applied to the sample via electrical contact and the resistance of the specimen could be measured [48–50]. Combined with magnetic field applied during electrical measurement, magnetotransport measurement is presented as an example shown in figure 11. Additionally, several steps of microfabrication to produce device and electrical contacts on the specimen are required [12, 51, 52].

*In situ* magnetoresistance measurement in Lorentz TEM have been reported by many authors [12, 47, 51–54]. Figure 12 demonstrates a study of micromagnetic behaviour of a NiFe element, patterned film grown on a SiN membrane substrate using *in situ* Lorentz microscopy in TEM during *in situ* magnetoresistance measurement (figure 12(a)) by Haug *et al* [53]. From $-40\,\mathrm{kA\,m^{-1}}$ up to the remanent state, the resistance appeared unchanged thus it can be seen via the Fresnel images (figures 12(i)–(iii)) that the structure was saturated. The edge fringes indicated that the magnetization was aligning along the negative y direction. This also could be visible via DPC image of magnetic induction. At a magnetic field of $4\,\mathrm{kA\,m^{-1}}$, the first signs of a magnetic domain on the right-hand side of the constriction could be observed (figure 12(iv)). The Fresnel image displayed the appearance of a bright and a dark wall in the wider stripe, and the corresponding DPC image showed a light bright contrast in this region. This domain enlarged under increasing magnetic field and could be seen both in the Fresnel and in the DPC images corresponding to data point (v) at a magnetic field of $6\,\mathrm{kA\,m^{-1}}$. Because the magnetization in NiFe film never changes abruptly but varies steadily, the appearance of a magnetic domain always involves the one of a magnetization component normal to the saturation direction. In that case, the magnetic domain results in an increase in the

x-component of the magnetization and therefore a respective decrease in the y component. As a result, the AMR theory could explain the reduction in the resistance in term of the appearance of the magnetic domain. As further increasing the field, the magnetization of the wider stripe switched to the opposite direction whereas the magnetization in the narrower stripe kept aligning along the negative y direction at a field of $8.6\,\mathrm{kA\,m^{-1}}$ (figure 12(vi)). Hence, the domain in the wider vanished, and the resistance appeared increasing slightly. However, it could not reach the starting value because of a magnetic domain created in narrower side of the device- the left-hand side of the constriction. It was apparently seen in the DPC image as a slight bright shadow at the left of the constriction; the corresponding domain walls could be observed in the Fresnel image. Furthermore, a tiny magnetic domain was pinned at the left upper edge of the wider side. This domain was eliminated as increasing the field to $12\,\mathrm{kA\,m^{-1}}$ (figure 12(vii) and (viii)), whereas the magnetic domain in the narrower stripe was expanded. Despite of rather small size, the domain located directly in the current path, and therefore it decreased the resistance to a minimum value. When the magnetization of the narrower strip was switched at $12.4\,\mathrm{kA\,m^{-1}}$ (figure 12(ix)), all magnetic domains were vanished to form the state which was saturated along the positive y direction. As a result, the measured resistance dropped back to approximately the starting value and remained unchanged under application of higher fields (figure 12(x)) [53].

Furthermore, combination of *in situ* LTEM and magnetoresistance reveals interesting aspect of domain wall resistance and spin-transfer torque effect [52, 53]. Figure 13 presents an example of probing spin-torque efficiency in NiFe nanobridge (as described in figures 9 and 10) [40, 52]. The

Adv. Nat. Sci.: Nanosci. Nanotechnol. **7** (2016) 045001

Review
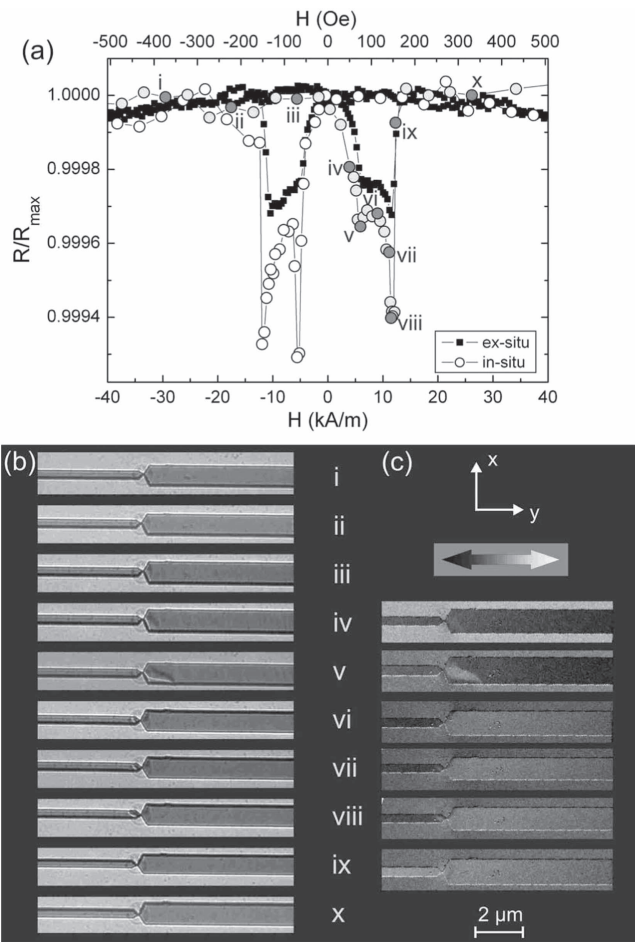


**Figure 12.** *In situ* magnetoresistance measurement and *in situ* Lorentz microscopy [53]: (a) magnetoresistance measured in *in situ* and *ex-situ* experiments on TEM; (b) and (c) structure of domains and domain walls in devices captured by Lorentz TEM under *in situ* magnetoresistance measurement. Figure is reproduced under permission of APS Publishing.

NiFe nanobridge device described in figures 9 and 10 was made again for *in situ* measurement of magnetotransport and TEM imaging in which the bridge connecting the two pads was 300 nm wide and 900 nm long. A system of Ti/Au contacts for transport were added by a further optical lithography lift-off step, and MR measurements were carried out using a standard lock-in detection method implemented with domain imaging using the DPC mode of Lorentz STEM. It was clearly seen that the magnetotransport measurements were very sensitive to the magnetic state in the region of the bridge. The magnetic induction vector maps constructed from DPC Lorentz STEM images are illustrated in figures 13(a)–(e). It was shown that the magnetization in the bridge was averagely canted at an angle of $\theta = -48° \pm 10°$ to the vertical direction leading to regions of domain-wall-like rotation of the magnetization at either end, with the thickness of several tens nanometres. In the subsequent remanent state (figure 13(b)), while the pads remain unswitched, the magnetization in the bridge was relaxed to lie more closely along its axis: $\theta = -2° \pm 6°$ and horn-shaped regions of canted magnetization extend from the bridge into the pads. Further reversing the field, the elliptical pad switched (figure 13(c)) showing a wall pinned at the bridge to reach high resistance state of the device which could be detected via the resistance measurement.

It was reported previously that the MR effect due to magnetic switching in such devices is not from intrinsic domain wall magnetoresistance (DWMR) [55], but essentially due to the anisotropic magnetoresistance (AMR) [44]. Thus, most of resistance arose in the nanobridge itself making the measurement to be a nanomagnetometer. By correlating the vanishing of AMR effect at high current density in the device with the deviation of the magnetisation induction from the DPC Lorentz STEM image, the spin-transfer efficiency, defined as the rate change of the switching field with the
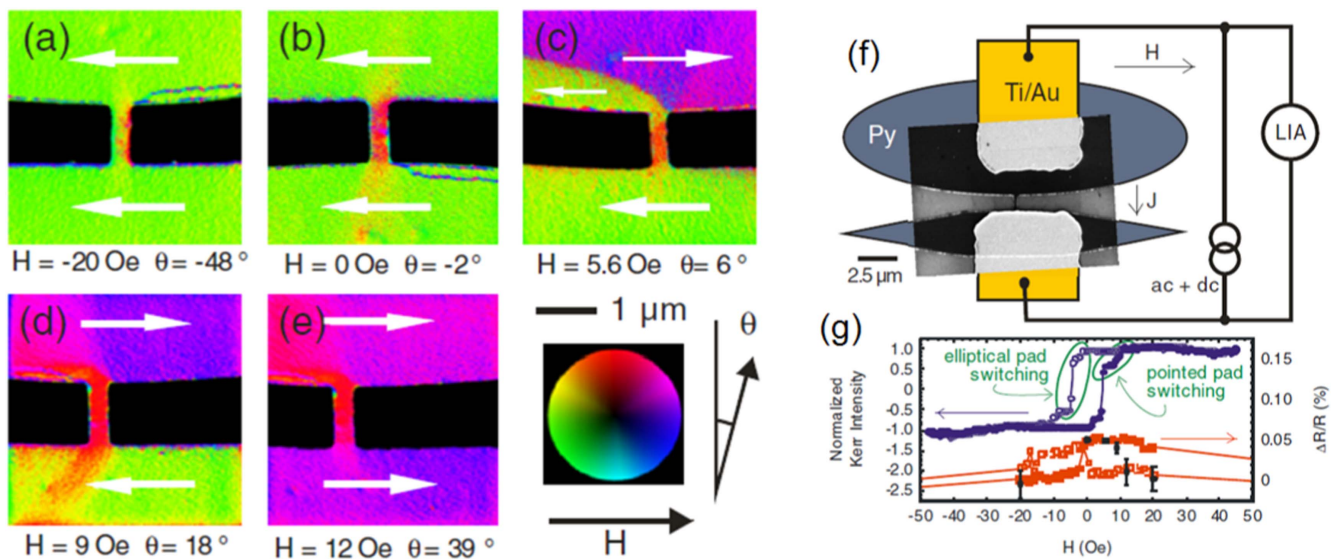


**Figure 13.** Measurement of spin-torque efficiency of a NiFe nanobridge by combining *in situ* STEM DPC Lorentz microscopy and magnetoresistance measurement [52]: (a)–(e) magnetisation configuration observed by DPC STEM LTEM at various applied field, (f) device structure for measurement and characterisation which was previously described in figures 9 and 10; (g) hysteresis loop and magnetoresistance results. Figure is reproduced under permission of AIP Publishing.
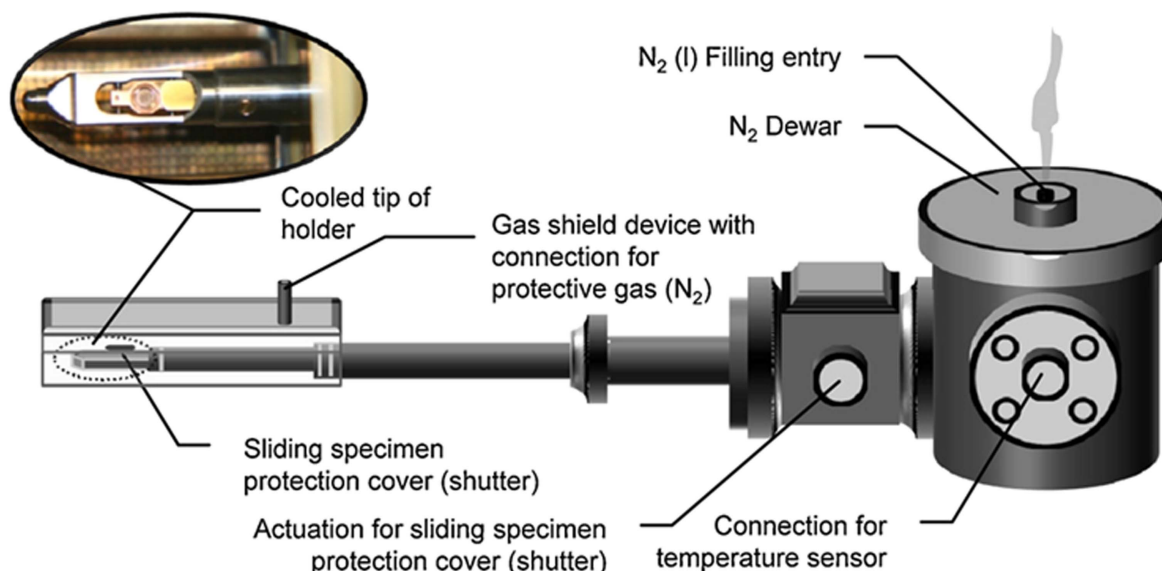
**Figure 14.** TEM heating holder for low-temperature controlling using liquid gaseous [58]: cooling is conducted using liquid nitrogen and temperature can be controlled by following gas and heating. Figure is reproduced under permission of Elsevier Ltd.

current density, $\xi = dH_{sw}/dJ_{dc}$ was determined to be $0.027 \pm 0.001$ Oe MA$^{-1}$ cm$^{-2}$ [52].

### 3.3. In situ observation of thermomagnetic dynamics in Lorentz TEM

Study of thermomagnetic dynamics is very important for understanding magnetic phase transition behaviour in magnetic materials, especially in magnetocaloric materials for magnetic refrigeration applications. For *in situ* study in TEM, a specimen holder with temperature-controlled stage is required, such as a heating holder for high temperature experiment [56], or cooling holder (cryo-holder) for low temperature work [57]. Figure 14 shows examples cooling TEM holder for low-temperature controlling experiments in TEM chamber.

The heating holder is similar to a biasing holder (see figure 11) with a microfurnace to heat the sample on the holder by the electrical current. Temperature at the sample stage is precisely detected by microsensor and controlled using an electronic controller. A cooling holder is working based on cryogenic liquid gas, such as liquid nitrogen, liquid helium that cools the specimen holder below the room temperature. Temperature can be changed using a microheater combined in the holder.

Thermally-induced first-order magnetic transition in La(Fe$_x$Si$_{1-x}$)$_{13}$ compounds was investigated by *in situ* Lorentz TEM in Fresnel mode [59]. Figure 15 demonstrates a typical picture of the thermomagnetic dynamics in the materials. This was described as [59]: in a temperature range, sufficiently below Curie temperature T$_C$ (stage labelled I in figure 15(a)), the magnetic domains were stable indicating no appreciable temperature dependence. On heating the sample with a temperature increasing rate of $1.14$ K min$^{-1}$, the domain configuration was modified in the temperature range II. This temperature range was likely quite narrow and was

located in the vicinity of the Curie temperature. The domain configuration changed stepwise in such a narrow temperature range II: figures 15(b) → (c) → (d). As the clear magnetic domain structure was observed in both figures 15(c) and (d), the viewing area was obviously in the ferromagnetic phase. The subsequent change was observed to be elimination of the domain structure referred to the temperature range III and figure 15(e). The domain wall motion at T$_C$ was too fast to observe using camera. For instance, the bright lines as indicated by the arrows in figure 15(e) stemmed from one magnetic domain wall, which was migrating downward, and its stepwise motion was faster than the TV-rate of $1/30$ s thereby the two bright lines were recorded in this frame. Once the reverse transformation to the paramagnetic phase was completed, the Fresnel image showed no contrasts related to magnetism in figure 15(f), revealing only bend contours. The observation showed a discontinuous change in the long-range order parameter (magnetisation) at T$_C$. It should be noted that the disappearance of magnetic domains was accompanied by a substantial change in the volume denoted by the diffraction contrast of TEM images, e.g., position of bend contours (figure 15(f)), dramatically changed at the same time of the disappearance of magnetic domains. These were believed to be the characteristic features of the first-order phase transitions as the second-order magnetic phase transitions should show a gradual change in magnetic domain structures due to a moderate temperature dependence of magnetic moment.

Using the Lorentz microscopy observations, faint changes in the magnetic domain configuration prior to the disappearance of the magnetic domains were observed [59–61]. This configuration change has not been fully understood yet since it is a challenge to rule out the artifact, e.g., the configuration change is probably supposed to be a consequence of the phase transition occurred already in other portions of the specimen. It is considered as a challenging problem to discuss the fluctuations near the first-order magnetic phase
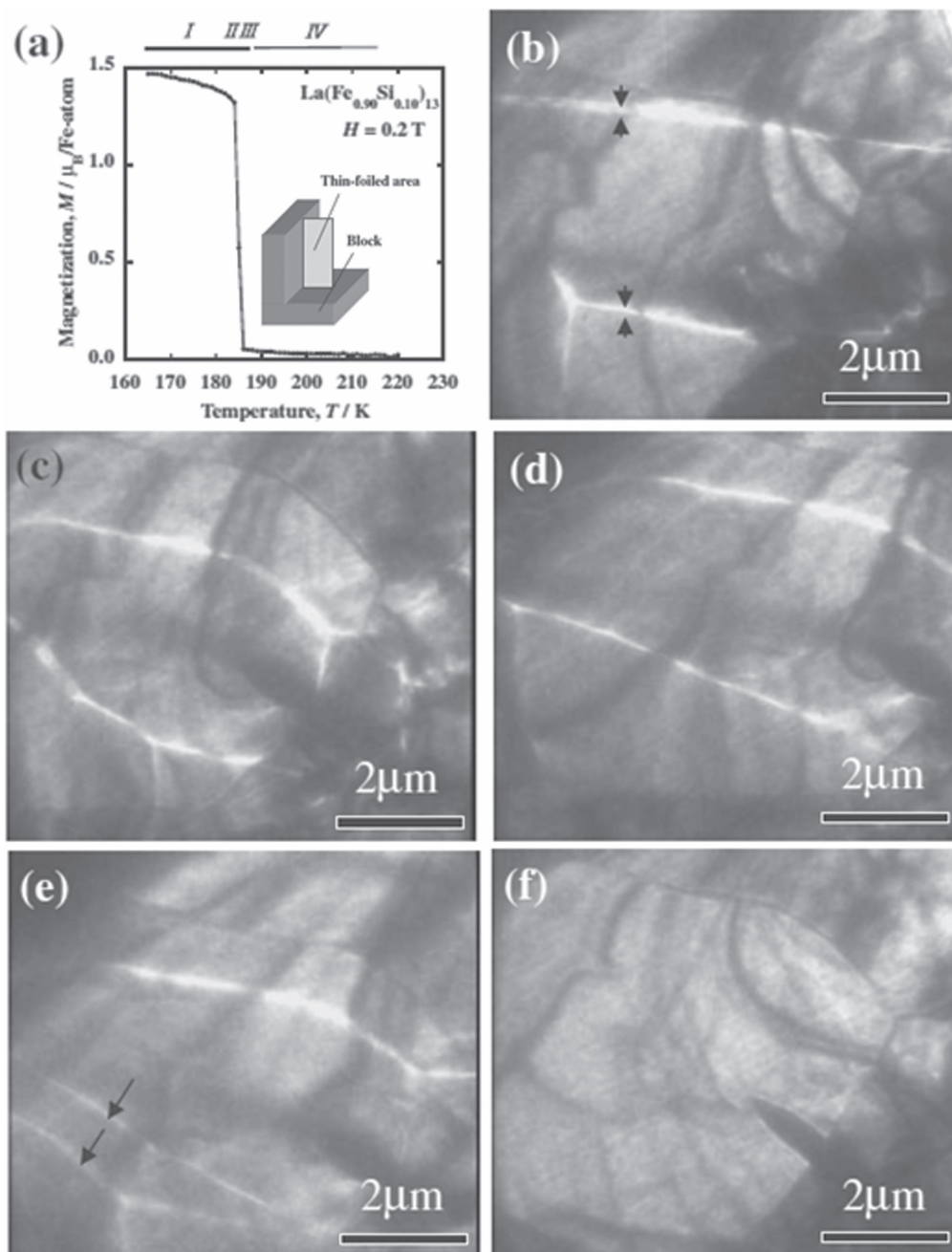
**Figure 15.** First-order phase transition in a La(Fe$_{0.90}$Si$_{0.10}$)$_{13}$ compound: (a) thermomagnetic curve measured on heating in a magnetic field of 0.2 T, (b)–(f) domain structure change during heating showing ferromagnetic-paramagnetic phase transition [59]. Figure is reproduced under permission of The Japan Institute of Metals and Materials.

transition [59]. *In situ* observation using Lorentz TEM is an effective approach to the critical phenomena of phase transitions.

Murakami *et al* [62] performed an *in situ* electron holography at low temperature to observed mixed phase state and magnetic phase transition in La$_{1-x}$Sr$_x$MnO$_3$ (x = 0.54, 0.56), and some typical results are demonstrated in figure 16. The holographic phase showed that, in the absence of a magnetic field, the magnetic flux was closed within ferromagnetic (FM) regions, indicating a negligible magnetic interaction between separated ferromagnetic domains. The volume of the FM region appeared to increase by formation of new magnetic

domains and their growth upon heating until the whole specimen became FM (figures 16(c)–(h)). A noticeable feature was obvious that the magnetic flux was closed within the FM region at every transformation from antiferromagnetic (AFM) to ferromagnetic (FM) phases. This resulted in a negligible magnetic interaction between separated FM islands without applied magnetic field. The transformation from FM phase to AFM phases occurred in the opposite way to that described above. The upper panel of figure 16(i) indicates the phase shift along the line X–Y in figure 16(g) which appeared to increase linearly in the FM region. The spatial distribution of magnetization could be assessed by using the differential of
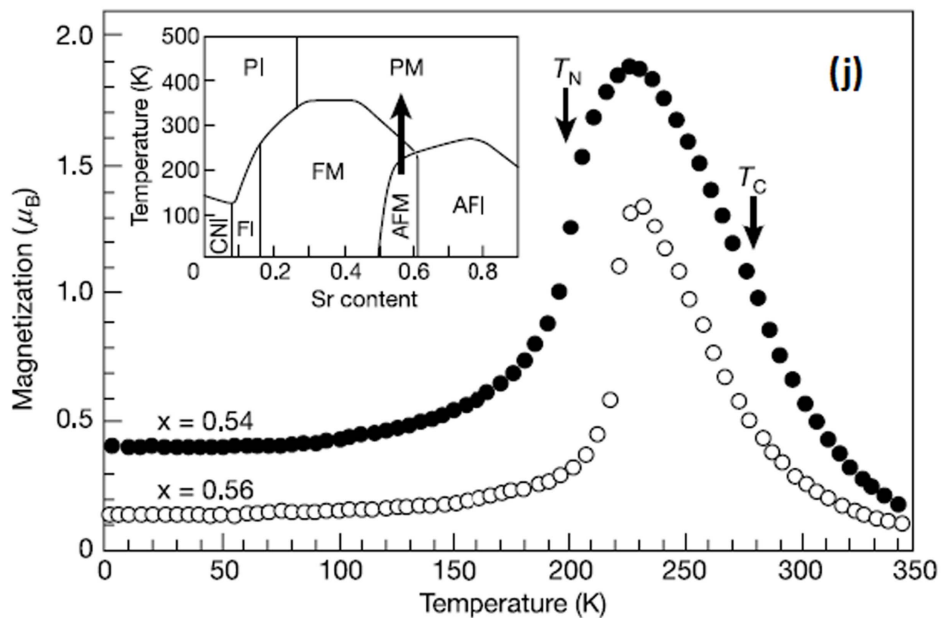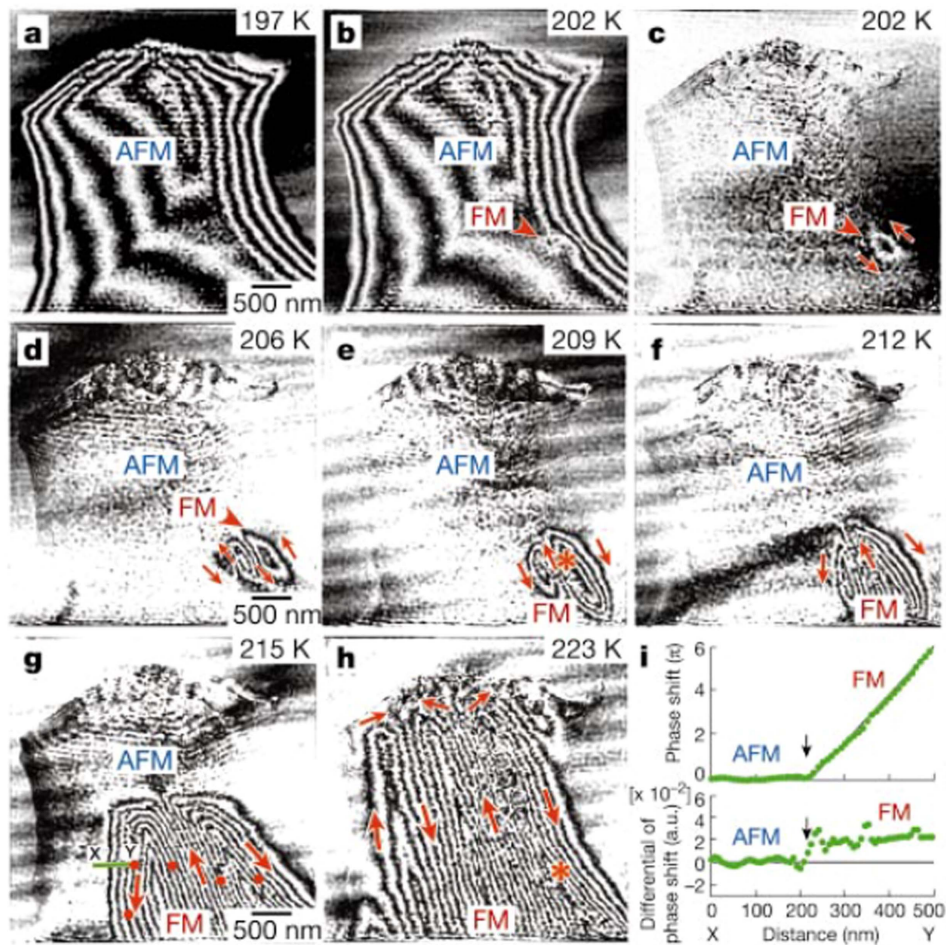
**Figure 16.** Temperature dependence of the magnetic microstructure in the mixed-phase (ferromagnetic and antiferromagnetic) state in $La_{1-x}Sr_xMnO_3$ [62]: (a)–(b) magnetic structure of the sample at various temperatures around Néel temperature. Direction of lines of magnetic flux (black-and-white lines in (c)–(h) is indicated by red arrows. The upper panel of (i) illustrates the phase shift along the line X–Y in (g). The lower panel of (i) demonstrates the differential of the phase shift. The plots in (j) shows temperature dependence of magnetisation. The figure is reproduced under permission of Nature Publishing.

the phase shift (figure 16(i), lower panel). Both the plateau on the right side, and the steep drop denoted by the arrow, indicated uniform magnetization over the FM region, but it abruptly diminishes at the interface with the AFM region. The work reviewed here revealed that there was only a negligible magnetic interaction between well-separated FM islands, but these islands were believed to interact with each other under application of magnetic fields. It was believed that the *in situ* magnetic structure observations would help understanding the physical processes underlying colossal magnetoresistive phenomena in perovskite materials [62].

## 4. Conclusions and outlooks

Transmission electron microscopy (TEM) for magnetic imaging, Lorentz microscopy, is a superior technique to observe magnetic structure in thin specimens of magnetic materials with high spatial resolution up to few nanometres. Together with excellent spatial resolution, good temporal resolution allows many types of *in situ* experiments to be performed inside the TEM chamber. Thanks to the development of microfabrication of specimen holders and TEM specimens, Lorentz TEM and electron holography has become unique and powerful techniques to study micromagnetic behaviour dynamically under *in situ* experiments, including *in situ* magnetisation, magnetotransport measurements, as well as thermomagnetic dynamics. The capability of performing *in situ* experiments inside the TEM chamber allows correlating the change in the magnetic properties, the magnetic phase with the change in the physical structure (morphology, crystallography and composition) as well as the micromagnetic structure and micromagnetic behaviour at nanoscale. With development of the aberration-corrected Lorentz STEM, sub-nanometre resolved images of magnetic structure could be resolved in fantastic *in situ* experiments.

## Acknowledgments

## References

[1] Žutić I, Fabian J and Sarma S D 2004 *Rev. Mod. Phys.* **76** 323
[2] Fusil S, Garcia V, Barthélémy A and Bibes M 2014 *Annu. Rev. Mater. Res.* **44** 91
[3] Fert A 2008 *Rev. Mod. Phys.* **80** 1517
[4] Grünberg P A 2008 *Rev. Mod. Phys.* **80** 1531
[5] Bader S D 2006 *Rev. Mod. Phys.* **78** 1
[6] Wang Z L 2003 *Adv. Mater.* **15** 1497
[7] Spence J C H 1999 *Mater. Sci. Eng. R Reports* **26** 1
[8] Krivanek O L, Lovejoy T C and Dellby N 2015 *J. Microsc.* **259** 165
[9] Sigle W 2005 *Annu. Rev. Mater. Res.* **35** 329
[10] Chapman J N 1984 *J. Phys. D: Appl. Phys.* **17** 623
[11] Lichte H *et al* 2007 *Annu. Rev. Mater. Res.* **37** 539
[12] Ngo D-T 2010 Lorentz TEM characterisation of magnetic and physical structure of nanostructure magnetic thin films *PhD Thesis* University of Glasgow
[13] Chapman J N *et al* 1994 *IEEE Trans. Magn.* **30** 4479
[14] Rodríguez L A *et al* 2013 *Ultramicroscopy* **134** 144
[15] Petford-Long A K and Chapman J N 2005 *Magnetic Microscopy of Nanostructures* ed H Hopster and H P Oepen (New York: Springer) pp 67–86
[16] Tanase M and Petford-Long A K 2009 *Microscopy Research and Technique* **72** 187
[17] Leaver K D 1968 *Thin Solid Films* **2** 149
[18] Podbrdsky J 1974 *J. Microsc.* **101** 231
[19] McVitie S *et al* 2015 *Ultramicroscopy* **152** 57
[20] Chapman J N, Batson P E, Waddell E M and Ferrier R P 1978 *Ultramicroscopy* **3** 203
[21] Chapman J N, Ploessl R and Donnet D M 1992 *Ultramicroscopy* **47** 331
[22] Linck M, Freitag B, Kujawa S, Lehmann M and Niermann T 2012 *Ultramicroscopy* **116** 13
[23] Gabor D 1948 *Nature* **161** 777
[24] Haine M E and Mulvey T 1952 *J. Opt. Soc. Am.* **42** 763
[25] Koch C T 2014 *Micron* **63** 69
[26] Tonomura A 1992 *Adv. Phys.* **41** 59
[27] Midgley P 2001 *Micron* **32** 167
[28] Ngo D-T and McVitie S 2011 *Ultramicroscopy* **111** 1276
[29] Lau J W, Schofield M A and Zhu Y 2007 *Ultramicroscopy* **107** 396
[30] Arita M, Tokuda R, Hamada K and Takahashi Y 2014 *Mater. Trans.* **55** 403
[31] Mcvitie S and Hefferman S J 1988 *J. Phys. C* **8** 1817
[32] Hefferman S J and Chapman J N 1990 *J. Magn. Magn. Mater.* **83** 223
[33] Daboo C *et al* 1995 *Phys. Rev. B* **51** 15964
[34] Petford-Long A K, Portier X, Tsymbal E Y, Anthony T C and Brug J A 1999 *IEEE Trans. Magn.* **35** 788
[35] Yu A C C, Petford-Long A K and Miyazaki T 2001 *Jpn. J. Appl. Phys.* **40** 4891
[36] Varón M *et al* 2015 *Sci. Rep.* **5** 14536
[37] Ngo D-T *et al* 2011 *J. Phys. D: Appl. Phys.* **44** 095001
[38] Hehn M *et al* 2008 3 *Appl. Phys. Lett.* **92** 072501
[39] Hoffmann H 1968 *IEEE Trans. Magn.* **4** 32
[40] Ngo D-T *et al* 2011 *IEEE Trans. Magn.* **47** 2511
[41] Kirk K J, Chapman J N and Wilkinson C D W 1999 *J. Appl. Phys.* **85** 5237
[42] Schneider M, Hoffmann H and Zweck J 2000 *Appl. Phys. Lett.* **77** 2909
[43] Petit D *et al* 2010 *Appl. Phys. Lett.* **97** 233102
[44] Hickey M C, Atkinson D, Marrows C H and Hickey B J 2008 *J. Appl. Phys.* **103** 07D518
[45] Asaka T *et al* 2002 *Phys. Rev. Lett.* **89** 207203
[46] He J Q *et al* 2010 *Phys. Rev. B—Condens. Matter Mater. Phys.* **81** 094427
[47] Li Y *et al* 2013 *Phys. Rev. Lett.* **110** 1
[48] Canepa S, Alam S B, Ngo D-T, Ross F M and Mølhave K 2016 *Controlled Atmosphere Electron Microscopy* ed T W Hansen and J B Wagner (Switzerland: Springer) pp 281–300
[49] Bernal R A, Ramachandramoorthy R and Espinosa H D 2015 *Ultramicroscopy* **156** 23
[50] Arita M, Hamada K, Takahashi Y, Sueoka K and Shibayama T 2015 *The Transmission Electron Microscope—Theory and Applications* ed K Maaz (Rijeka: InTech) pp 35–68

Adv. Nat. Sci.: Nanosci. Nanotechnol. **7** (2016) 045001

Review

[51] Portier X, Petford-Long A K, Doole R C, Anthony T C and Brug J A 1997 *IEEE Trans. Magn.* **33** 3574
[52] Hickey M C *et al* 2010 *Appl. Phys. Lett.* **97** 202505
[53] Haug T, Perzlmaier K and Back C H 2009 *Phys. Rev. B* **79** 1
[54] Petford-Long A K, Portier X, Bayle-Guillemaud P, Anthony T and Brug J 1998 *Microsc. Microanal.* **4** 325
[55] Marrows C H and Dalton B C 2004 *Phys. Rev. Lett.* **92** 097206
[56] Saka H, Kamino T, Ara S and Sasaki K 2008 *MRS Bull.* **33** 93
[57] Rajeswari J *et al* 2015 *Proc. Natl. Acad. Sci.* **112** 201513343
[58] Kuntsche J, Horst J C and Bunjes H 2011 *Int. J. Pharm.* **417** 120
[59] Kawamoto N *et al* 2005 *Mater. Trans.* **46** 1764
[60] Marshall A F *et al* 1999 *J. Appl. Phys.* **85** 4131
[61] Kawamoto N *et al* 2007 *J. Magn. Magn. Mater.* **310** 2815
[62] Murakami Y, Yoo J H, Shindo D, Atou T and Kikuchi M 2003 *Nature* **423** 965